



Cite this: *J. Mater. Chem. C*, 2018, **6**, 2573

Received 18th January 2018,
Accepted 16th February 2018

DOI: 10.1039/c8tc00288f

rsc.li/materials-c

Broadband hybrid organic/CuInSe₂ quantum dot photodetectors†

Ruiqi Guo, Ting Shen and Jianjun Tian *

“Green” narrow band-gap CuInSe₂ quantum dots (QDs) were first introduced in photodetectors. Thus, a broadband hybrid photodetector was obtained by combining the ultraviolet detection of spiro-OMeTAD and the near-infrared detection of CuInSe₂ QDs. In order to improve the detection of the device, the oil-soluble CuInSe₂ QDs were transformed into water-soluble MPA-capped QDs through ligand exchange, which drastically shortened the length of the surface ligand. The specific detectivity (D^*) of the photodetector reached 1.6×10^{12} Jones at 330 nm and 7.5×10^{10} Jones at a 1000 nm wavelength. The unencapsulated device also displayed a fast response time (<0.02 s) and excellent thermal stability (20–100 °C) in ambient air. This work could open a window of toxic-free QD based photodetectors to achieve a broadband response.

1 Introduction

Quantum dots (QDs) have attracted much attention in recent years due to their unique physical characteristics. Such as with the quantum size effect,^{1–3} the bandgap of the nanostructured material is strongly dependent on the size of the QDs. Therefore, the light response region of devices can be adjusted by controlling the size of the QDs. In addition, rapid advances in photoelectrical applications as light-absorbing materials, coupled with high extinction coefficients and multiple exciton generation,^{4–8} make them more widely used.^{2,9–21} Nowadays, there is an urgent need to explore the interaction between light and materials, especially semiconductor materials achieved through various photodetector devices.²² Recently, near-infrared detectors have become a hot research topic due to their numerous applications including thermal imaging, spectroscopy, optical communication and medical imaging.^{23,24} Near-infrared photodetectors are capable of transforming low-energy infrared photons into an electrical signal. Traditional photodetectors are made using single crystalline materials such as silicon and III-V semiconductors. Colloidal QDs can be prepared for photodetectors by a solution process, and show a superiority of low-cost in comparison with traditional devices. Narrow band-gap QDs such as PbS QDs^{20,22,23,25–30} and PbSe QDs^{31,32} have shown a great vitality for near-infrared photodetectors. For example, Sargent *et al.*, using the structure of quantum-dot-in-perovskite photodetectors,²⁵ achieved a response into the near-infrared and specific detectivities that exceed 10^{12} Jones.

However, the drawback of these materials is the toxic Pb element. Apart from PbS and PbSe QDs, narrow band-gap CdTe QD based photodetectors also achieved specific detectivity (D^*) of 5×10^{17} Jones, which was the highest value for all visible and infrared photodetectors at room temperature.³³ Huo *et al.* fabricated a photodetector by integrating the material with MoS₂–HgTe QDs and achieved a high responsivity (R) of 10^6 A W⁻¹.¹⁷ As above, the key problem is the toxic elements^{34,35} (Cd or Hg), which cause a big hindrance to the development and applications of QD photodetectors. Therefore, it is crucial to find toxic-free QDs and apply them to photodetectors.

The rapid emergence of “green” QDs^{5,36,37} has received tremendous interest, such as MA₃Bi₂Br₉,⁵ Cs₃Bi₂Br₉,³⁷ and CuInS₂.³⁸ However, their absorption can only reach the visible range and it is difficult to meet the requirements of near-infrared photodetectors. In addition, their performance is far from that of Cd and Pb chalcogen QDs. CuInSe₂ is derived from CuInS₂ and is superior to CuInS₂ QDs in that it has a narrower bandgap and a wider absorption range.^{36,39,40} The CuInSe₂ QDs are candidates to replace Pb chalcogen QDs and they are a promising material for “green” QD near-infrared photodetectors.

In our previous work,⁴¹ spiro-OMeTAD not only served as a hole transport material for heterojunctions, but also had a high responsivity and detectivity in the ultraviolet range. Here, we designed a broadband photodetector by combining the ultraviolet detection of spiro-OMeTAD and the near-infrared detection of CuInSe₂ QDs. The configuration of the detector was assembled according to FTO/compact TiO₂ thin layer/mesoporous TiO₂ layer/CuInSe₂ QD layer/spiro-OMeTAD/Ag. However, the detection performance of the device was much lower in the near-infrared region due to poor charge transport of the QD layer. Several strategies have been studied to enhance the “green” QD

Institute for Advanced Materials and Technology, University of Science and Technology Beijing, 100083, China. E-mail: tianjianjun@mater.ustb.edu.cn

† Electronic supplementary information (ESI) available. See DOI: 10.1039/c8tc00288f

stability and luminous properties. For example, different ligands, like oleyl amine and oleic acid, are used to control the crystallization and stability of QDs. Hence, OAm-capped CuInSe₂ QDs were transformed to MPA-capped CuInSe₂ QDs by ligand exchange resulting in the photodetector showing excellent broadband detection in the range of ultraviolet to near infra-red. The detectivity of the MPA-CuInSe₂ QD based photodetector reached 1.6×10^{12} Jones at 330 nm and 7.5×10^{10} Jones at 1000 nm.

2 Experimental details

2.1 Materials

Copper iodide (CuI, 99.998%), indium acetate (In(OAc)₃, 99.99%), 1-octadecene (ODE, 90%) and 3-mercaptopropionic acid (MPA, 97%) were obtained from Alfa Aesar. Selenium powder (200 mesh, 99.99%) and oleylamine (OAm, 90%) were obtained from Aladdin and diphenylphosphine (DPP, 98%) was purchased from J&K. All chemicals were used directly without further processing.

2.2 Synthesis of CuInSe₂ QDs

The DPP-Se precursor was obtained by dispersing 0.3 mmol Se powder in 0.3 ml DPP and 0.5 ml OAm by sonication to form a clear bright yellow solution. For a typical synthesis, 0.1 mmol CuI, 0.1 mmol In(OAc)₃, 2 ml OAm and 2 ml ODE were loaded into a 50 ml three-necked flask. After stirring and argon bubbling at room temperature for 20 min, the mixture was heated to 110 °C while stirring under vacuum for 5 min. The system was then heated to a set temperature (120, 160 and 200 °C), followed by injection of the Se precursor prepared as above. After growth for 5 min, the temperature was cooled to 90 °C for further precipitation and dispersion. 10 ml of hexane was added and CuInSe₂ QDs were precipitated with excess ethanol and acetone and then centrifuged at 4000 rpm for 1 min. OAm-capped CuInSe₂ QD precipitate was dissolved in dichloromethane, and phase transfer reagent MPA was used to get the MPA-capped water-soluble CuInSe₂ QDs. After that, MPA-capped CuInSe₂ QDs were dispersed in 1 ml deionized water for further use.

2.3 Fabrication of photodetector devices

FTO glasses were successively cleaned by deionized water, acetone and alcohol solvents for 45 min followed by a 7 min UV-ozone treatment. Compact TiO₂ was coated on the FTO by the spray pyrolysis method under ambient conditions, followed by annealing at 450 °C for 30 min as in previous reports.^{42–47} The thickness of the compact TiO₂ layer is around 20 nm. Afterwards, mesoporous TiO₂ was spin-coated on the compact TiO₂ layer with a speed of 4000 rpm and heated at 450 °C for 30 min. In this work, CuInSe₂ QDs were spin-coated after heating. The chlorobenzene solution containing spiro-OMeTAD (72.3 mg ml⁻¹), *tert*-butyl pyridine (28.8 μl ml⁻¹) and Li-TFSI (17.5 μl ml⁻¹), was spin-coated as a hole transfer layer at 4000 rpm for 30 s.⁴⁸ An Ag counter electrode was fabricated by thermal evaporation. The effective area was 0.1007 cm².

2.4 Characterization

The UV-vis absorption was measured using an ultraviolet-visible (UV-vis) spectrophotometer (UV-3600, Shimadzu). The structures of the materials were identified using X-ray diffraction (XRD) (Rigaku, D/max-RB) with a Cu K α wave. The transmission electron microscopy (TEM) and high-resolution transmission electron microscopy (HRTEM) images were obtained on a JEM-2010. The current-voltage curves were recorded using a digital source meter (2400, Keithley Instruments Inc.) under 3 A grade AM 1.5G simulated sunlight (100 mW cm⁻²) (7-SS1503A, 7 Star Optical Instruments Co., Beijing, China). The responsivity and EQE were measured in direct current (DC) mode using a custom measurement system consisting of a 150 W xenon lamp (7ILX150A, 7 Star Optical Instruments Co., Beijing, China), a monochromator (7ISW30, 7 Star Optical Instruments Co., Beijing, China) and a digital source meter (2400, Keithley Instruments Inc.). The responses of open circuit voltage, current and responsivity spectra were measured from an electrochemical workstation.

3 Results and discussion

CuInSe₂ QDs were prepared by hot-injection at different reaction temperatures (120, 160 and 200 °C) and were then used to assemble photodetectors as shown in Fig. S1–S5 (ESI[†]). As the reaction temperature increased, the size of the quantum dots grew and the absorption edge red shifted, due to quantum confinement. When the temperature was 200 °C, the size of the QDs increased by 5.3 nm. The absorption onset of the QDs extended accordingly. When the synthesis temperature exceeded 200 °C, the result was no QDs due to the overgrowth of crystals. Fig. 1(a) shows high resolution transmission electron microscopy (HRTEM) of CuInSe₂ QDs synthesized at 200 °C. The clear lattice fringes correspond to (112) and (220) lattice planes. Fig. 1(b) shows the X-ray diffraction (XRD) patterns of CuInSe₂ QDs and the red bars show characteristic diffraction patterns for chalcopyrite according to JCPDS# 40-1487. The XRD patterns indicate the (112), (220) and (312) planes of the tetragonal phase CuInSe₂ QDs, which is also confirmed by Fig. 1(a). The absorption spectrum for CuInSe₂ QDs as shown in Fig. 1(c) shows the absorption onset extending to 1100 nm, making it a potential candidate for fabricating a near-infrared photodetector. The Fig. 1(c) inset diagram shows a Tauc plot and is used to determine the band gap of CuInSe₂ QDs. The bandgap value for CuInSe₂ QDs, synthesized at 200 °C, can be determined as 1.24 eV. As shown in Fig. S2(c) (ESI[†]), the band gaps of CuInSe₂ QDs synthesized at 120 °C and 160 °C are 1.72 eV and 1.33 eV, respectively. The EQE results of the hybrid organic/CuInSe₂ QD photodetectors illustrate that the photodetector based on 200 °C CuInSe₂ QDs has the widest response range of up to 1100 nm (Fig. S5(a), ESI[†]). Therefore, CuInSe₂ QDs prepared at 200 °C show the broadest absorption region (1100 nm) and an excellent detection performance. Later in the study, we mainly explored the CuInSe₂ QDs synthesized at 200 °C for photodetectors. To achieve a broadband photodetector, spiro-OMeTAD was introduced as a hole transport

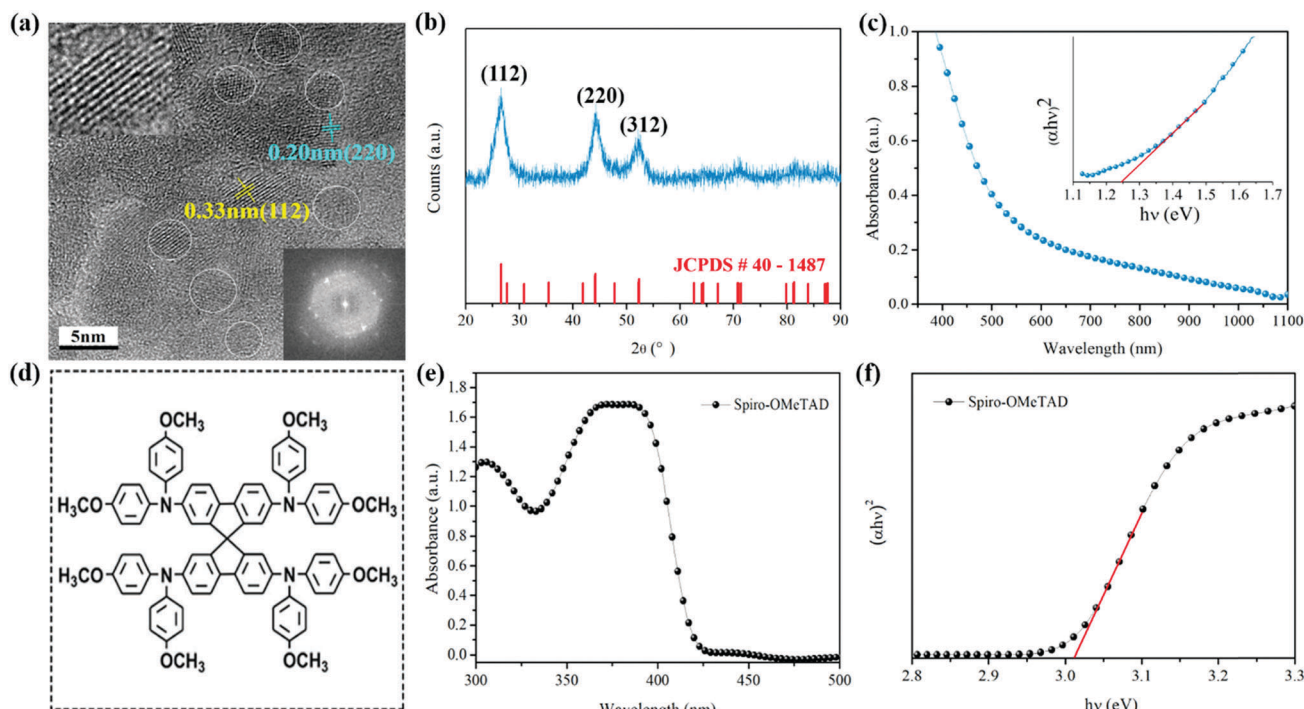


Fig. 1 (a) HRTEM micrograph, (b) the reference XRD patterns and (c) absorption spectrum of CuInSe_2 QDs synthesized at 200°C , inset diagram shows a Tauc plot used to determine the band gap of 200°C CuInSe_2 QDs. (d) The chemical formula and (e) the absorption spectra of spiro-OMeTAD. (f) Tauc plot used to determine the band gap of spiro-OMeTAD.

and ultraviolet detection material. Fig. 1(d) shows the chemical formula of spiro-OMeTAD. The spiro-OMeTAD not only provides excellent extraction and transport of holes, but also shows

obvious photovoltaic performance.⁴⁹ Therefore, spiro-OMeTAD has been widely used in solar cells^{44,45} and photodetectors.^{41,50} Fig. 1(e) shows the absorption spectrum of the spiro-OMeTAD

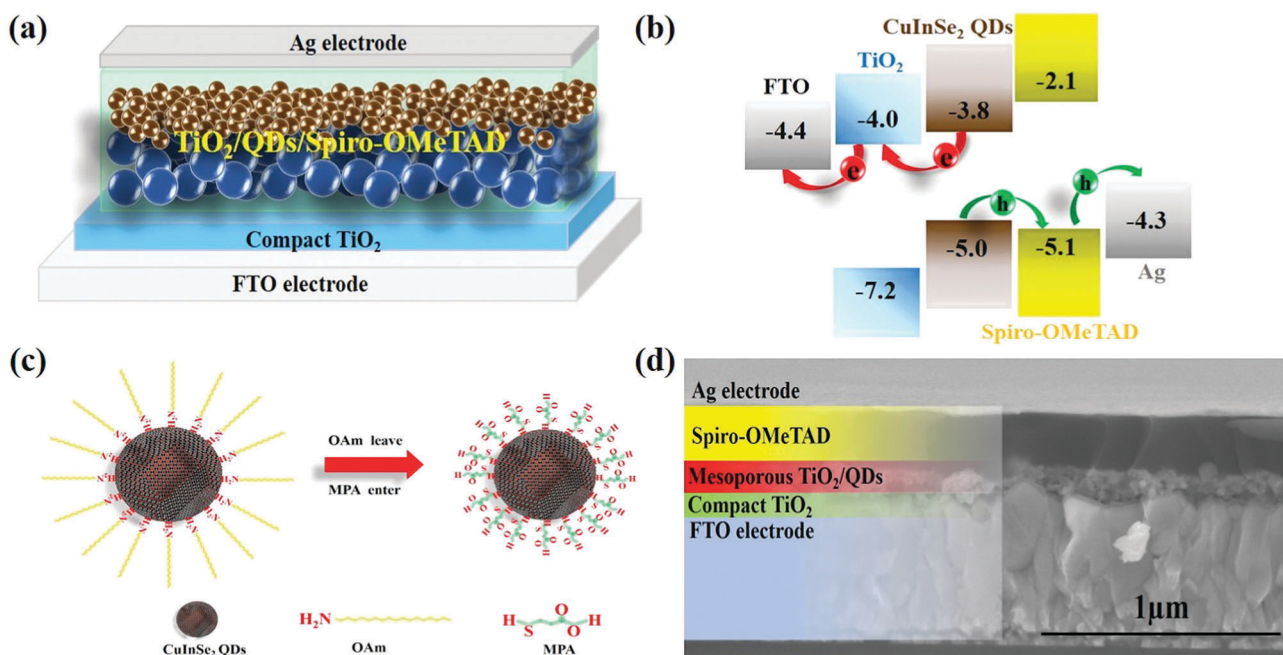


Fig. 2 (a) The device structure of the photodetector with the CuInSe_2 QD layer, (b) the energy diagram of the photodetector, (c) the ligand exchange process from OAm-capped oil-soluble CuInSe_2 QDs to MPA-capped water-soluble CuInSe_2 QDs and (d) a cross-sectional SEM image of the device with MPA- CuInSe_2 QD layers.

film, indicating the highest absorbance at 370 nm. According to an extrapolation of the Tauc plot in Fig. 1(f), a bandgap value for spiro-OMeTAD can be determined as 3.01 eV.

Fig. 2(a) shows the photodetector configuration, which is constructed as FTO/compact TiO_2 layer/mesoporous TiO_2 layer/ CuInSe_2 QD layer/spiro-OMeTAD layer/Ag. Fig. 2(b) displays the energy diagram of the CuInSe_2 QD photodetector. The CuInSe_2 QDs absorb photons and then yield excitons (hole–electron pairs). The holes are transferred by spiro-OMeTAD to reach the Ag electrode, while the electrons are transferred through the mesoporous TiO_2 and compact TiO_2 to the FTO electrode. The QDs were usually obtained by hot-injection synthesis using an oil-based solvent. The oil-soluble QDs are capped by long carbon chain ligands, which greatly suppress the charge transport. To improve the charge transport through the QD layer, the long ligands could be replaced by short-chained bifunctional linker molecules through a ligand exchange process.⁵¹ Here, we propose a strategy to obtain water-soluble QDs capped by bifunctional linker molecules. Fig. 2(c) shows the ligand exchange process from OAm-capped oil-soluble CuInSe_2 QDs to MPA-capped water-soluble CuInSe_2 QDs. This type of exchange is commonly referred to as *ex situ* ligand exchange. This method, as presented in the Experimental section, allows a more efficient ligand exchange process and obtains higher-performance QDs. Fig. 2(d) shows the cross-sectional SEM image of the device with MPA- CuInSe_2 QD layers. The boundaries of each layer in the device are very clear, indicating high charge carrier transport.

Photocurrent density–voltage and dark current density–voltage curves of the photodetector are given in Fig. 3(a) and (b), respectively. The phenomenon that the minimum current value does not occur at zero is called the zero-offset voltage, resulting from the photovoltaic effect and asymmetric structure. For a CuInSe_2 QD photodetector, CuInSe_2 QDs produce carriers by photons, which move to the right to form a charge current under the electric field, resulting in a zero offset. In addition, the load of QDs also affects the photocurrent, which is the reason for the voltage offset. After introducing the MPA- CuInSe_2 QD layer, the ratio of photocurrent density to dark current density

increases from 188 to 417 at 0 V. The main reason is attributed to a high loading of MPA- CuInSe_2 QDs within the film. Fig. S7 (ESI†) shows that the absorption intensity of the MPA- CuInSe_2 QDs/ TiO_2 film is higher than that of the OAm- CuInSe_2 QDs/ TiO_2 film. From the film color (Fig. S7(b and c), ESI†), it is clear that the adsorption capacity of MPA- CuInSe_2 QDs on the electron transport layer is much higher than that of OAm- CuInSe_2 QDs. Consequently, the noise interference of the MPA- CuInSe_2 QD layer detected is smaller than that of the OAm- CuInSe_2 QD layer. Thus, overall, the MPA- CuInSe_2 QD based photodetector performs better in noise immunity and detection capability than the other one.

Fig. 4(a) shows the photocurrent density–time response of the OAm- CuInSe_2 QD and MPA- CuInSe_2 QD based photodetectors. The current density of the MPA- CuInSe_2 QD based photodetector is three times larger than that of the OAm- CuInSe_2 QD based one. Fig. 4(b) exhibits the rise and decay time of the devices. The rise time (t_r) is defined as the photocurrent increase from 10% to 90% of the peak output value, and the decay time (t_d) is defined as the decrease from 90% to 10% of the peak value. It is clear that both the rise time and decay time of the MPA- CuInSe_2 QD photodetectors are less than 0.04 s, and are much shorter than those of the OAm-QD device. The rise time and decay time of the OAm- CuInSe_2 QD photodetectors are 0.08 s and 0.15 s, respectively. Overall, the MPA- CuInSe_2 QD detector responds much faster than the OAm- CuInSe_2 QD device. However, the current density of the MPA- CuInSe_2 QD based photodetector is not stable owing to the surface defects of QDs. The long-chain ligands of the QD surface were replaced with short-chain ligands that resulted in the increase of the surface defects. So, the carriers will continuously fill the defects under illumination.

An important measure of the photodetector performance is responsivity (R). Responsivity corresponds to the ratio of photocurrent to incident light density. The responsivity spectra of the two structured photodetectors are shown in Fig. 5(a). The two types of device can both respond in the ultraviolet region. However, the response of the OAm-QD based photodetector in the visible and near-infrared regions is very weak. After ligand exchange

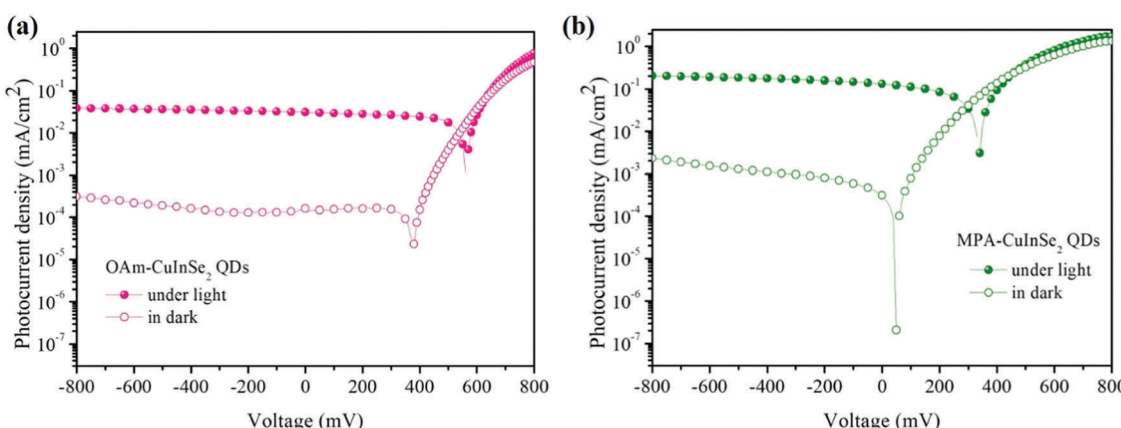


Fig. 3 Logarithmic form of photocurrent density–voltage and dark current density–voltage curves for (a) OAm- CuInSe_2 QD based photodetector and (b) MPA- CuInSe_2 QD based photodetector measured under 100 W m^{-2} light density.

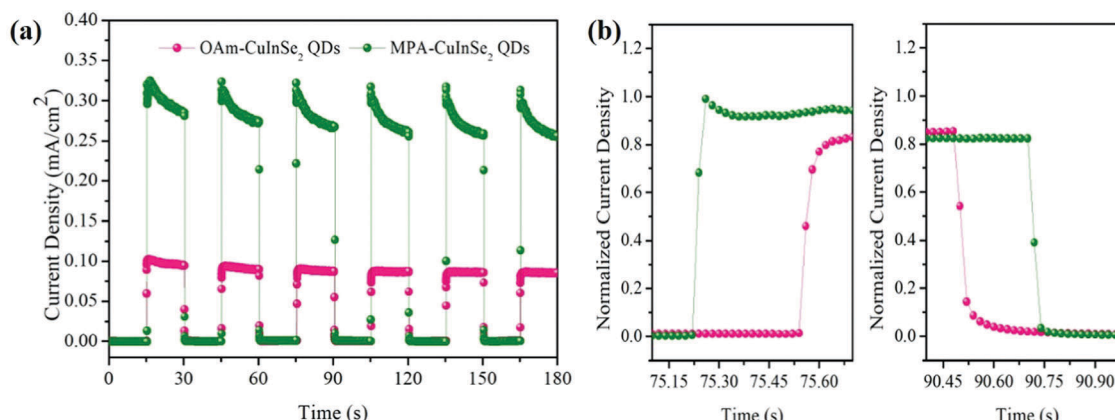


Fig. 4 (a) Photocurrent density–time response of OAm–CuInSe₂ QD and MPA–CuInSe₂ QD photodetectors measured under 100 W m⁻² light density. (b) Rise and decay time of the photodetector devices.

with MPA, the response of the photodetector in the visible and near infrared region is improved. The response in the ultra-violet region is mainly due to the spiro-OMeTAD as described in our previous work,⁴¹ while the response of the visible and near-infrared region is mainly due to the dominant effect of the CuInSe₂ QDs. Fig. 5(b) shows the specific detectivity (D^*) of the OAm–CuInSe₂ QD and MPA–CuInSe₂ QD photodetectors within 300–1100 nm, calculated at 0 V bias voltage. D^* can be calculated by the equation:

$$D^* = R_\lambda \frac{1}{\sqrt{(2qJ_d)}} \quad (1)$$

where R_λ is the responsivity at the wavelength of λ , q is the elementary charge and J_d is the dark current.⁴¹ D^* is an important indicator for the light-detecting ability of a photodetector. The results show that the detectivity of the photodetector assembled by MPA–CuInSe₂ QDs in the visible and near-infrared region is significantly higher than that of the OAm-capped oil-soluble CuInSe₂ QD device. The detectivity of the MPA–CuInSe₂ QD based photodetector can reach 1.6 × 10¹² Jones (1 Jones = 1 cm Hz^{1/2} W⁻¹) in the ultraviolet light

region at 0 V and surpasses 10¹¹ Jones in the near infrared region. In addition, the response range of the device can cover the entire near-infrared region. The detection performance of the devices in different regions is summarized in Table 1. On the basis of the results, we know that the detection performance of the devices can be greatly improved through ligand exchange from OAm to MPA, which means MPA–CuInSe₂ QD devices have a higher photosensitivity in characterizing the signal levels. As the surface ligand acts as an insulator, the short-length ligand would increase the charge transport of the QD layer. In addition, the water-soluble QDs are easily absorbed by the TiO₂ layer. The amount of adhesion of QDs in the device also increases, leading to high responsivity and detectivity.

Fig. 6(a) illustrates the responsivity of the device with MPA–CuInSe₂ QD layers at different temperatures: 20 °C, 60 °C, 80 °C and 100 °C. When the temperature increases, the responsivity of the photodetector fluctuates slightly in the near-infrared region but still responds in the entire near-infrared region. Interestingly, the response of the device fluctuates as the temperature increases in the visible region, while the response maintains a relatively constant value in the near-infrared region.

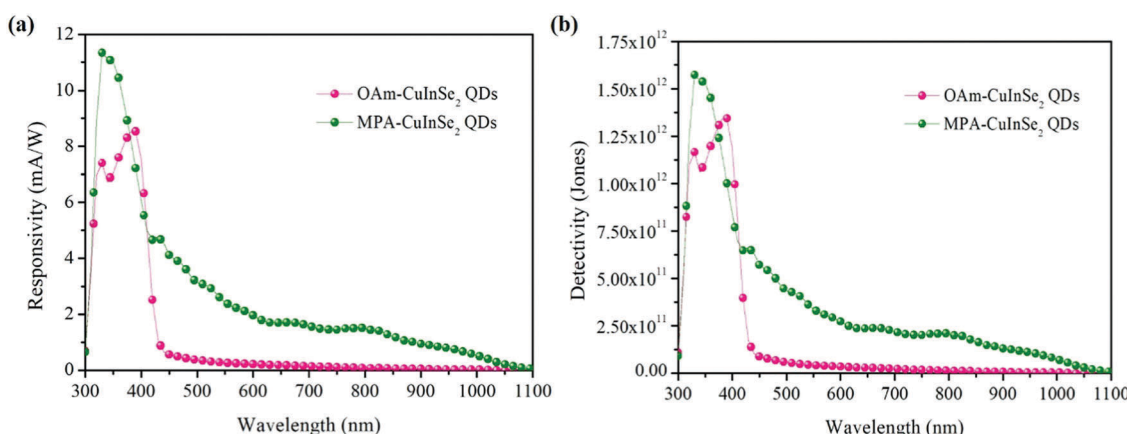
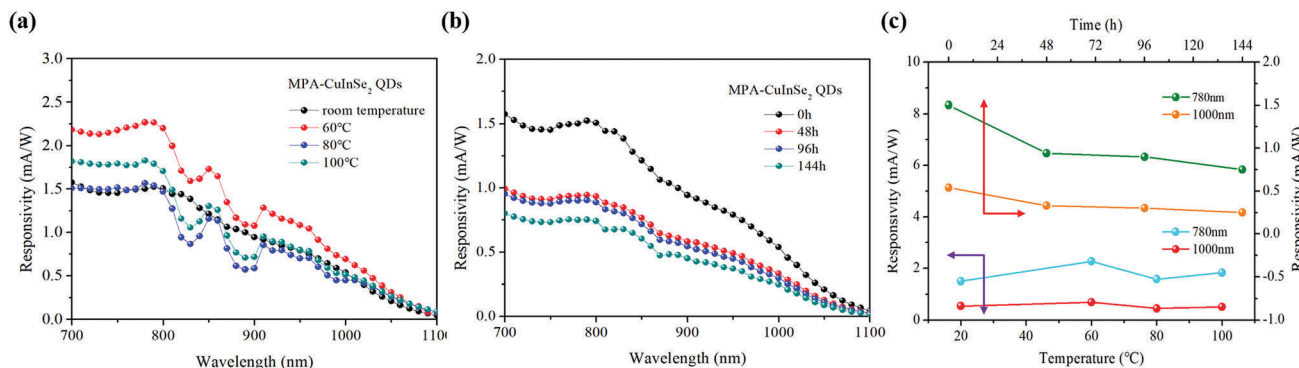


Fig. 5 (a) Spectroscopic response and (b) specific detectivity of the OAm–CuInSe₂ QD and MPA–CuInSe₂ QD based photodetectors with a wavelength of illumination from 300 to 1100 nm, calculated at 0 V bias voltage.

Table 1 The detectivity and responsivity of the OAm–CuInSe₂ QD and MPA–CuInSe₂ QD based photodetectors at different wavelengths

Photodetectors	Detection	Optical wave			
		330 nm	500 nm	780 nm	1000 nm
OAm–QD layer	D^* (Jones)	1.2×10^{12}	5.8×10^{10}	1.4×10^{10}	3.7×10^9
MPA–QD layer	D^* (Jones)	1.6×10^{12}	4.4×10^{11}	2.1×10^{11}	7.5×10^{10}
OAm–QD layer	R (mA W ⁻¹)	7.4	0.4	0.1	—
MPA–QD layer	R (mA W ⁻¹)	11.3	3.1	1.5	0.5

**Fig. 6** The responsivity of the device with the MPA–CuInSe₂ QD layers at (a) different temperatures of 20 °C (room temperature), 60 °C, 80 °C and 100 °C. (b) Various storage time durations of 0 hours, 48 hours, 96 hours and 144 hours in ambient air. (c) 780 nm and 1000 nm under different conditions.

Remarkably, the response of the device increases as the temperature rises to 60 °C. The possible reason is attributed to a decrease in defects among different interfaces. Fig. 6(b) shows the responsivity of the unencapsulated device with MPA–CuInSe₂ QDs stored in ambient air for 0 hours, 48 hours, 96 hours and 144 hours. With an increase in storage time, the responsivity of the device declines slightly. Compared to the visible region, the responsivity of the detector in the near-infrared region is maintained at an almost invariable level after a storage time for 48 hours. According to Fig. 6(c), the responsivity of the device under different conditions can be maintained at an almost invariable level, demonstrating that the thermal and time stabilities of these devices are excellent.

4 Conclusions

Toxic-free “green” CuInSe₂ QDs were obtained by hot-injection, which showed a wide light absorption range to near infrared (~ 1100 nm). As a hole transport and ultraviolet detection material, spiro-OMeTAD was introduced to the CuInSe₂ QD based photodetector. This hybrid organic/CuInSe₂ QD photodetector exhibited broadband detection in the range of ultraviolet to near infrared. The conventional oil-soluble OAm-capped CuInSe₂ QDs were transformed to water-soluble MPA-capped QDs through ligand exchange, which drastically shortened the length of the surface ligand improving the charge transport in the QD layer. The detection performance of the device improved accordingly. The detectivity of the MPA–CuInSe₂ QD based photodetector reached to 1.6×10^{12} Jones at 330 nm and over 10^{11} Jones in the near-infrared region. In addition, the device displayed an excellent thermal stability at 20–100 °C. Therefore, as a kind of

non-poisonous material, CuInSe₂ QDs are well suited to achieve a broadband response.

Conflicts of interest

The authors declare no competing financial interests.

Acknowledgements

This work was supported by the National Science Foundation of China (51774034, 51772026 and 51611130063), Beijing Natural Science Foundation (2182039), Fundamental Research Funds for the Central Universities (FRF-BD-16-012A) and 111 Project (No. B17003).

References

- 1 J. Y. Kim, O. Voznyy, D. Zhitomirsky and E. H. Sargent, *Adv. Mater.*, 2013, **25**, 4986–5010.
- 2 M. R. Kim and D. Ma, *J. Phys. Chem. Lett.*, 2015, **6**, 85–99.
- 3 J. Tian, L. Lv, C. Fei, Y. Wang, X. Liu and G. Cao, *J. Mater. Chem. A*, 2014, **2**, 19653–19659.
- 4 J. Zhang, Y. Yang, H. Deng, U. Farooq, X. Yang, J. Khan, J. Tang and H. Song, *ACS Nano*, 2017, **11**, 9294–9302.
- 5 M. Leng, Z. Chen, Y. Yang, Z. Li, K. Zeng, K. Li, G. Niu, Y. He, Q. Zhou and J. Tang, *Angew. Chem., Int. Ed.*, 2016, **55**, 15012–15016.
- 6 X. Li, Y. Wang, H. Sun and H. Zeng, *Adv. Mater.*, 2017, **29**, 1701185.

- 7 J. Tian, E. Uchaker, Q. Zhang and G. Cao, *ACS Appl. Mater. Interfaces*, 2014, **6**, 4466–4472.
- 8 J. Tian, Q. Zhang, E. Uchaker, Z. Liang, R. Gao, X. Qu, S. Zhang and G. Cao, *J. Mater. Chem. A*, 2013, **1**, 6770–6775.
- 9 S. Ruhle, M. Shalom and A. Zaban, *ChemPhysChem*, 2010, **11**, 2290–2304.
- 10 S. Cao, J. Zheng, J. Zhao, Z. Yang, C. Li, X. Guan, W. Yang, M. Shang and T. Wu, *ACS Appl. Mater. Interfaces*, 2017, **9**, 15605–15614.
- 11 X. Dai, Y. Deng, X. Peng and Y. Jin, *Adv. Mater.*, 2017, **29**, 1607022.
- 12 Z. Shi, Y. Li, Y. Zhang, Y. Chen, X. Li, D. Wu, T. Xu, C. Shan and G. Du, *Nano Lett.*, 2017, **17**, 313–321.
- 13 Y. Wang, X. Bai, T. Wang, L. Yan, T. Zhang, Y. Zhang and W. W. Yu, *Nanotechnology*, 2017, **28**, 215703.
- 14 H. Zou, M. Liu, D. Zhou, X. Zhang, Y. Liu, B. Yang and H. Zhang, *J. Phys. Chem. C*, 2017, **121**, 5313–5323.
- 15 X. Li, Y. Wu, S. Zhang, B. Cai, Y. Gu, J. Song and H. Zeng, *Adv. Funct. Mater.*, 2016, **26**, 2435–2445.
- 16 Y. Zhang, G. Hong, Y. Zhang, G. Chen, F. Li, H. Dai and Q. Wang, *ACS Nano*, 2012, **6**, 3695–3702.
- 17 N. Huo, S. Gupta and G. Konstantatos, *Adv. Mater.*, 2017, **29**, 1606576.
- 18 Z. Zheng, F. Zhuge, Y. Wang, J. Zhang, L. Gan, X. Zhou, H. Li and T. Zhai, *Adv. Funct. Mater.*, 2017, **27**, 1703115.
- 19 M. Chen, H. Lu, N. M. Abdelazim, Y. Zhu, Z. Wang, W. Ren, S. V. Kershaw, A. L. Rogach and N. Zhao, *ACS Nano*, 2017, **11**, 5614–5622.
- 20 L. Gao, C. Chen, K. Zeng, C. Ge, D. Yang, H. Song and J. Tang, *Light: Sci. Appl.*, 2016, **5**, e16126.
- 21 Y. Huang, X. Zhan, K. Xu, L. Yin, Z. Cheng, C. Jiang, Z. Wang and J. He, *Appl. Phys. Lett.*, 2016, **108**, 013101.
- 22 R. Saran and R. J. Curry, *Nat. Photonics*, 2016, **10**, 81–92.
- 23 A. A. Bessonov, M. Allen, Y. Liu, S. Malik, J. Bottomley, A. Rushton, I. Medina-Salazar, M. Voutilainen, S. Kallioinen, A. Colli, C. Bower, P. Andrew and T. Ryhanen, *ACS Nano*, 2017, **11**, 5547–5557.
- 24 A. Rogalski, *Prog. Quantum Electron.*, 2003, **27**, 59–210.
- 25 F. P. Garcia de Arquer, X. Gong, R. P. Sabatini, M. Liu, G. H. Kim, B. R. Sutherland, O. Voznyy, J. Xu, Y. Pang, S. Hoogland, D. Sinton and E. Sargent, *Nat. Commun.*, 2017, **8**, 14757.
- 26 S. A. McDonald, G. Konstantatos, S. Zhang, P. W. Cyr, E. J. Klem, L. Levina and E. H. Sargent, *Nat. Mater.*, 2005, **4**, 138–142.
- 27 D. K. Hwang, Y. T. Lee, H. S. Lee, Y. J. Lee, S. H. Shokouh, J.-h. Kyhm, J. Lee, H. H. Kim, T.-H. Yoo, S. H. Nam, D. I. Son, B.-K. Ju, M.-C. Park, J. D. Song, W. K. Choi and S. Im, *NPG Asia Mater.*, 2016, **8**, e233.
- 28 J. P. Clifford, G. Konstantatos, K. W. Johnston, S. Hoogland, L. Levina and E. H. Sargent, *Nat. Nanotechnol.*, 2009, **4**, 40–44.
- 29 G. Konstantatos, L. Levina, A. Fischer and E. H. Sargent, *Nano Lett.*, 2008, **8**, 1446–1450.
- 30 Z. Ren, J. Sun, X. Zhong, J. Hu, S. Yang and J. Wang, *Adv. Mater.*, 2017, **29**, 1702055.
- 31 G. I. Koleilat, L. Levina, H. Shukla, S. H. Myrskog, S. Hinds, A. G. Pattantyus-Abraham and E. H. Sargent, *ACS Nano*, 2008, **2**, 833–840.
- 32 J. Gao, S. C. Nguyen, N. D. Bronstein and A. P. Alivisatos, *ACS Photonics*, 2016, **3**, 1217–1222.
- 33 Y. Zhang, D. J. Hellebusch, N. D. Bronstein, C. Ko, D. F. Ogletree, M. Salmeron and A. P. Alivisatos, *Nat. Commun.*, 2016, **7**, 11924.
- 34 J. Zhou, M. Zhu, R. Meng, H. Qin and X. Peng, *J. Am. Chem. Soc.*, 2017, **139**, 16556–16567.
- 35 T. Shen, L. Bian, B. Li, K. Zheng, T. Pullerits and J. Tian, *Appl. Phys. Lett.*, 2016, **108**, 213901.
- 36 W. Li, Z. Pan and X. Zhong, *J. Mater. Chem. A*, 2015, **3**, 1649–1655.
- 37 B. Yang, J. Chen, F. Hong, X. Mao, K. Zheng, S. Yang, Y. Li, T. Pullerits, W. Deng and K. Han, *Angew. Chem., Int. Ed. Engl.*, 2017, **56**, 12471–12475.
- 38 M. Mou, Y. Wu, Q. Niu, Y. Wang, Z. Yan and S. Liao, *Chem. Commun.*, 2017, **53**, 3357–3360.
- 39 M. G. Panthani, C. J. Stolle, D. K. Reid, D. J. Rhee, T. B. Harvey, V. A. Akhavan, Y. Yu and B. A. Korgel, *J. Phys. Chem. Lett.*, 2013, **4**, 2030–2034.
- 40 J. Du, Z. Du, J. S. Hu, Z. Pan, Q. Shen, J. Sun, D. Long, H. Dong, L. Sun, X. Zhong and L. J. Wan, *J. Am. Chem. Soc.*, 2016, **138**, 4201–4209.
- 41 H. Bai, T. Shen and J. Tian, *J. Mater. Chem. C*, 2017, **5**, 10543–10548.
- 42 M. M. Lee, J. Teuscher, T. Miyasaka, T. N. Murakami and H. J. Snaith, *Science*, 2012, **338**, 643–647.
- 43 W. Huang, F. Huang, E. Gann, Y.-B. Cheng and C. R. McNeill, *Adv. Funct. Mater.*, 2015, **25**, 5529–5536.
- 44 B. Li, M. Li, C. Fei, G. Cao and J. Tian, *J. Mater. Chem. A*, 2017, **5**, 24168–24177.
- 45 M. Li, B. Li, G. Cao and J. Tian, *J. Mater. Chem. A*, 2017, **5**, 21313–21319.
- 46 H. Bai, T. Shen, S. Wang, B. Li, G. Cao and J. Tian, *Sci. China Mater.*, 2017, **60**, 637–645.
- 47 T. Shen, J. Tian, B. Li and G. Cao, *Sci. China Mater.*, 2016, **59**, 833–841.
- 48 C. Fei, L. Guo, B. Li, R. Zhang, H. Fu, J. Tian and G. Cao, *Nano Energy*, 2016, **27**, 17–26.
- 49 N. J. Jeon, H. G. Lee, Y. C. Kim, J. Seo, J. H. Noh, J. Lee and S. I. Seok, *J. Am. Chem. Soc.*, 2014, **136**, 7837–7840.
- 50 D. Li, G. Dong, W. Li and L. Wang, *Sci. Rep.*, 2015, **5**, 7902.
- 51 S. Wang, C. Bi, J. Yuan, L. Zhang and J. Tian, *ACS Energy Lett.*, 2018, **3**, 245–251.